

# Kinetic Analysis of Hepatic Metabolism Using Hyperpolarized Dihydroxyacetone

Alexander Kirpich,<sup>†,‡,§,¶,||</sup> Mukundan Ragavan,<sup>§,○,||</sup> James A. Bankson,<sup>||,⊥</sup> Lauren M. McIntyre,<sup>#,¶,||</sup> and Matthew E. Merritt<sup>\*,§,§,||,||</sup>

<sup>†</sup>Department of Biology, University of Florida, Gainesville, Florida 32611, United States

<sup>‡</sup>Informatics Institute, University of Florida, Gainesville, Florida 32611, United States

<sup>¶</sup>Southeast Center for Integrated Metabolomics, University of Florida, Gainesville, Florida 32611, United States

<sup>§</sup>Department of Biochemistry and Molecular Biology, University of Florida, Gainesville, Florida 32611, United States

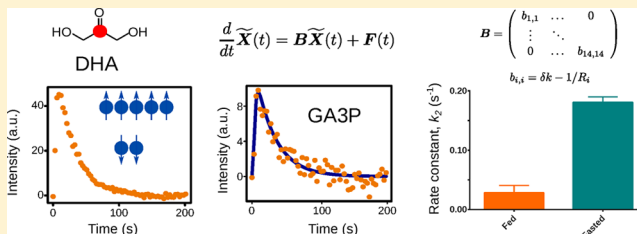
<sup>||</sup>Department of Imaging Physics, The University of Texas MD Anderson Cancer Center, Houston, Texas 77030, United States

<sup>⊥</sup>The University of Texas MD Anderson Cancer Center, UTHealth Graduate School of Biomedical Sciences, Houston, Texas 77030, United States

<sup>#</sup>Department of Molecular Genetics and Microbiology, University of Florida, Gainesville, Florida 32611, United States

## Supporting Information

**ABSTRACT:** Hyperpolarized carbon-13 magnetic resonance (HP-MR) is a new metabolic imaging method that does not use ionizing radiation. Due to the inherent chemical specificity of MR, not only tracer uptake but also downstream metabolism of the agent is detected in a straightforward manner. HP [2-<sup>13</sup>C] dihydroxyacetone (DHA) is a promising new agent that directly interrogates hepatic glucose metabolism. DHA has three metabolic fates in the liver: glucose production, glycerol production and potential inclusion into triglycerides, and oxidation in the tricarboxylic acid cycle. Each pathway is regulated by flux through multiple enzymes. Using Duhamel's formula, the kinetics of DHA metabolism is modeled, resulting in estimates of specific reaction rate constants. The multiple enzymatic steps that control DHA metabolism make more simplified methods for extracting kinetic data less than satisfactory. The described modeling paradigm effectively identifies changes in metabolism between gluconeogenic and glycogenolytic models of hepatic function.



## INTRODUCTION

<sup>1</sup>H nuclear magnetic resonance (NMR) spectroscopy can measure metabolite concentrations with great accuracy in serum, urine, and in cell and tissue extracts.<sup>1,2</sup> Magnetic resonance methods can also be adapted to monitor metabolic changes in different systems including *in vivo*. <sup>13</sup>C NMR measurements offer tremendous tracing capabilities<sup>3</sup> with relatively small background signal due to the low <sup>13</sup>C natural abundance. At the same time, measuring conventional <sup>13</sup>C spectra is time-consuming due to inherently low sensitivity.

Dissolution dynamic nuclear polarization (DNP) alleviates the lack of sensitivity by offering an NMR signal enhancement of greater than 10,000 fold in solution.<sup>4</sup> Additionally, DNP is agnostic about the type of chemical species (subject to certain spin relaxation requirements) and can be used to hyperpolarize different substrates and study various targets including heart, liver, and kidney. The advent of DNP has made it possible to follow metabolic reactions in tissues with temporal resolution of seconds using various substrates such as pyruvate,<sup>5–10</sup>

lactate,<sup>11</sup> butyrate,<sup>12,13</sup> acetoacetate,<sup>14</sup> and glutamine,<sup>15</sup> among others.<sup>16</sup>

Recently, [2-<sup>13</sup>C] dihydroxyacetone (DHA) was used to study liver metabolism. Results from the *ex vivo* model demonstrated that DHA metabolism was profoundly sensitive to the metabolic state of the liver.<sup>17</sup> DHA is a substrate that is rapidly metabolized by the liver and its first product of metabolism, dihydroxyacetone phosphate, is ideally situated at the midpoint of the Embden–Meyerhof–Parnas (EMP) pathway. DHA can be rapidly phosphorylated in the liver and participates in glycerogenesis, gluconeogenesis, and glycolysis thereby generating <sup>13</sup>C incorporation in both upstream and downstream metabolites including glucose-6-phosphate, fructose-6-phosphate, and phosphoenol pyruvate.

Hyperpolarized (HP) <sup>13</sup>C spectra that are recorded are a function of several dynamic processes including transport

Received: October 24, 2018

Published: January 2, 2019

phenomena (across the cellular and organelle membranes), reaction kinetics, and nuclear spin relaxation. Several models exist for analyzing kinetic data involving HP pyruvate.<sup>18–21</sup> However, the reaction kinetics and relaxation considerations of DHA are significantly more complex due to the sheer number of metabolites observed after HP DHA injection. In this work, we use the data presented in a prior study of liver metabolism using hyperpolarized DHA<sup>17</sup> to develop a mathematical formulation to describe HP data and extract kinetic parameters of various reactions that describe the EMP pathway.

## METHODS

**Hyperpolarized <sup>13</sup>C NMR Data.** We used the hyperpolarized <sup>13</sup>C NMR data published by Moreno et al.<sup>17</sup> for analysis in this work. The work involved *ex vivo* mouse liver perfusions in two dietary states—glycogenolytic (fed) and gluconeogenic (fasted). Hyperpolarized [2-<sup>13</sup>C] DHA was injected into mouse livers perfused to metabolic steady state. NMR data acquisition was carried out using 30° radio-frequency (RF) pulses at a magnetic field strength of 9.4 T.

**Data Preparation.** NMR spectra were processed and peak areas were obtained by integration as discussed in the prior publication.<sup>17</sup> Integrated peak areas were then scaled to the total spectral intensity of each spectrum.<sup>22</sup> In order to have a complete set of resonances (i.e., no missing metabolite resonances in any spectrum), white noise was generated and added for those metabolites that were missing in experiments where the metabolism was not favorable for their observation. The procedure for generating the missing values was as follows: Integrals were obtained for the region of interest in individual transients recorded between 117 and 147 s (a repetition time of 3 s yields 10 data points) from the start of the HP experiment. These transients can be safely assumed to contain only noise. Mean and standard deviation values were computed from these ten transients. Using the mean and standard deviation, independent and identically distributed (IID) Gaussian noise was generated and used as peak areas for missing resonances.

**Software.** All the analysis was performed using R software for statistical computing.<sup>23</sup> An exponential matrix function was used from the external library (`Matrix`). Libraries `matrixcalc` and `matrixStats` were used to make the computations and summaries easier. For the matrix inversion, `solve()` function was initially used but upon debugging, we found `qr.solve()` to be more reliable. The optimization and model fitting was performed using built-in R function `optim()`.

**Model Formulation in Matrix Form.** The dynamic processes involved in pyruvate–lactate exchange was modeled by a system of linear ordinary differential equations in matrix form.<sup>24</sup> The system has the matrix form:

$$\frac{d}{dt}\tilde{\mathbf{X}}(t) = \mathbf{B}\tilde{\mathbf{X}}(t) + \tilde{\mathbf{F}}(t) \text{ with initial condition } \tilde{\mathbf{X}}(0) = \tilde{\mathbf{X}}_0 \quad (1)$$

where  $\tilde{\mathbf{X}}(t)$  is a response vector function of dimension  $K \times 1$  describing the NMR spectra recorded,  $\frac{d\tilde{\mathbf{X}}(t)}{dt}$  is a vector of derivatives of dimension  $K \times 1$  with respect to time  $t$ ,  $\mathbf{B}$  is a  $K \times K$  matrix encompassing both reaction rate constants and spin relaxation rates, and  $\tilde{\mathbf{F}}(t)$  is a time-dependent vector

function that describes delivery of hyperpolarized substrates to the perfused organ.

To account for variations in signal intensity across experiments, each NMR spectrum is scaled to its total spectral intensity.<sup>22</sup> This scaling, denoted as  $s$ , implies  $X(t) = s\tilde{X}(t)$ ,  $F(t) = s\tilde{F}(t)$ , and the rescaled system of equations has the form:

$$\frac{d}{dt}\mathbf{X}(t) = \mathbf{B}\mathbf{X}(t) + \mathbf{F}(t) \text{ with initial condition } \mathbf{X}(0) = \mathbf{X}_0 \quad (2)$$

Spectra ( $X(t)$ ) are collected at equally spaced time points  $t_0, t_1, \dots, t_n$  for  $n = 0, 1, \dots, N$ . To model the data accurately, a denser set of points is defined such that  $T_m = T_0 + m\Delta$  where  $t_{n+1} - t_n = l\Delta$  for some positive value of  $l$  (for the experiments considered here,  $l = 3$  and  $\Delta = 1$  s). For convenience, it is assumed that  $t_0 = T_0 = 0$  as a starting point for the experiment and data acquisition. For simplicity of notation, the value of system  $X$  at data points  $T_m$  is defined as  $X(T_m) = X_{T_m} = X_m$ .

Spectra collected at each point  $\{t_n; n = 0, 1, \dots, N\}$  differ from each other primarily due to chemical kinetics and NMR spin–lattice relaxation. Therefore, NMR signal is modeled separately for each interval of length  $\Delta$  (defined above):

$$\frac{d}{dt}\mathbf{X}(t) = \mathbf{B}\mathbf{X}(t) + \mathbf{F}(t) \text{ for } t \in (T_m; T_{m+1}]$$

the initial condition  $\mathbf{X}(T_m) = \mathbf{X}_m$  (3)

The solution to the equation above comes from Duhamel's formula for each time point  $t$  within the defined interval and has the form

$$\mathbf{X}(t) = e^{\mathbf{B}(t-T_m)}\mathbf{X}(T_m) + \int_{T_m}^t e^{\mathbf{B}(t-s)}\mathbf{F}(s) ds$$

for  $t \in (T_m; T_{m+1}]$  (4)

The data acquisition scheme employed in the HP experiments utilizes constant small flip angle ( $\theta$ ) RF pulses at each point ( $t_n$ ), which converts a portion of longitudinal magnetization to observable transverse magnetization ( $\sin(\theta)$ ). The remaining longitudinal magnetization ( $\cos(\theta)$ ) is utilized in subsequent acquisitions. In order to account for this change in longitudinal magnetization during the course of experiment, each measurement of  $X(t)$  at time  $t = t_n = T_m$  is adjusted at the beginning of the next time step ( $t = t_{n+1}$ ) by multiplier  $\cos(\theta)$ . It follows that the observed signal at  $t = t_n$  is obtained by multiplying  $X(t)$  by  $\sin(\theta)$ . However, this adjustment is not required for the modeled data between the data acquisition intervals ( $t_n$  and  $t_{n+1}$ ) for all  $n = 0, 1, \dots, N$ . The adjusted solutions for time  $t \in (T_m; T_{m+1}]$  have the form:

$$\mathbf{X}(t) = e^{\mathbf{B}(t-T_m)}\mathbf{X}(T_m)C_m + \int_{T_m}^t e^{\mathbf{B}(t-s)}\mathbf{F}(s) ds$$

for  $t \in (T_m; T_{m+1}]$

where  $C_m = \begin{cases} \cos(\theta) & \text{if } m \in \mathbb{S} \\ 1 & \text{otherwise} \end{cases}$  (5)

The set of indices  $\mathbb{S}$  stands for the subset from  $\{m: m = 0, 1, \dots, M\}$  that contains the indices of the data collection points. More rigorously, this means that  $m \in \mathbb{S} \Leftrightarrow \exists n: T_m = t_n$ .

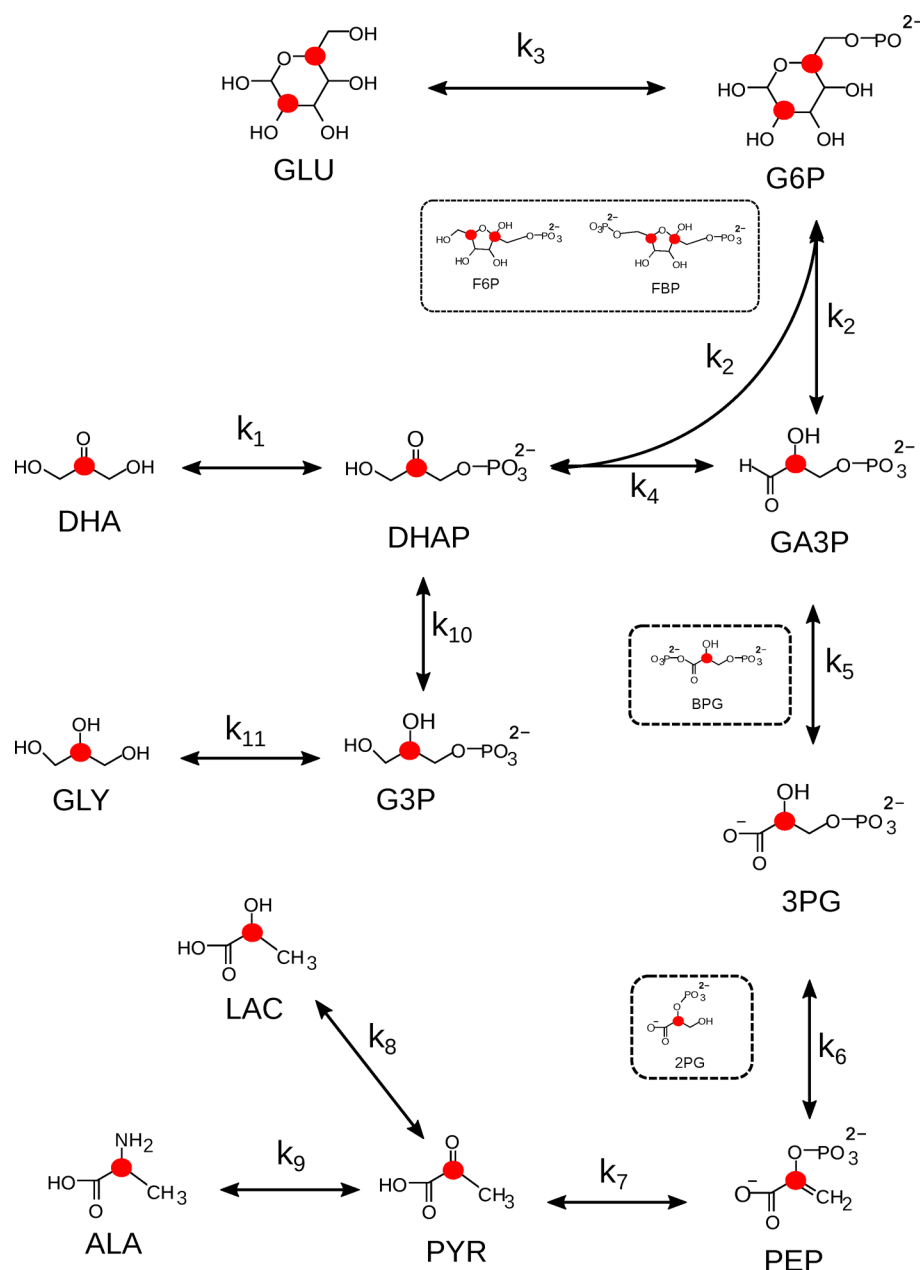


**Figure 1.** DHA metabolism shown with reaction rate constants. Metabolites not used in the model are encased in dashed box. Red filled circles indicate  $^{13}\text{C}$  label. Metabolites are abbreviated as follows: dihydroxyacetone DHA, Dihydroxyacetone phosphate DHAP, glycerol-3-phosphate G3P, glycerol: GLY, glyceraldehyde-3-phosphate GA3P, fructose-1,6-bisphosphate FBP, fructose-6-phosphate F6P, glucose-6-phosphate G6P, glucose GLU, 3-phosphoglycerate 3PG, 2-phosphoglycerate 2PG, phosphoenolpyruvate PEP, pyruvate PYR, alanine ALA, and lactate LAC.

**Model Solution.** The exact values that are produced by the model at time points  $X_{m+1}$  can be computed recursively from  $X_m$ . The computation depends on the value of matrix  $B$ , delivery function  $F(t)$ ,  $C_m$ , and the adjusted eq 5. The recursive formula has the form:

$$\mathbf{X}(T_{m+1}) = e^{B(T_{m+1}-T_m)}\mathbf{X}(T_m)C_m + \int_{T_m}^{T_{m+1}} e^{B(T_{m+1}-s)}F(s) ds \quad (6)$$

Further simplification is possible when  $F(t)$  is assumed to be (approximately) constant on time interval  $t \in (T_m; T_{m+1}]$ . In the simplified version of eq 6, the approximation  $F_m$  is used for  $F(s)$  ( $\forall s \in (T_m; T_{m+1}]$ ) together with notations

$\Delta = T_{m+1} - T_m$  and  $X_m = X(T_m)$ . The values of the system 6 at time points  $T_1, T_2, \dots, T_{m+1}$  have iterative relationships:

$$\begin{aligned} X_1 &= e^{B\Delta}X_0C_0 + [e^{B\Delta} - I]B^{-1}F_0 \\ X_2 &= e^{B\Delta}X_1C_1 + [e^{B\Delta} - I]B^{-1}F_1 \\ X_3 &= e^{B\Delta}X_2C_2 + [e^{B\Delta} - I]B^{-1}F_2 \\ &\dots \\ X_{m+1} &= e^{B\Delta}X_mC_m + [e^{B\Delta} - I]B^{-1}F_m \end{aligned} \quad (7)$$

Under the constant small flip angle scheme (described in the model formulation), measured spectra are related to the model formulation via the relationship  $Y_m = X_m \sin(\theta)$  or, equivalently

$X_m = Y_m/\sin(\theta)$  for  $m \in \mathbb{S}$ . The values  $Y_m$  are *not* measured for all indices  $m$  but only for those  $m \in \mathbb{S}$ . To simplify the notations analogously to  $C_m$  notations for  $S_m$  are introduced:

$$S_m = \begin{cases} \sin(\theta) & \text{if } m \in \mathbb{S} \\ 1 & \text{otherwise} \end{cases}$$

The notations for collected data simplify to  $Y_m = X_m S_m$  or  $X_m = Y_m/S_m$  and can be plugged into the equations to obtain recursive formula in terms of recorded data. The updated iterative relationship in terms of the recorded data have the form:

$$\begin{aligned} Y_1/S_1 &= e^{B\Delta}[Y_0/S_0]C_0 + [e^{B\Delta} - I]B^{-1}F_0 \\ Y_2/S_2 &= e^{B\Delta}[Y_1/S_1]C_1 + [e^{B\Delta} - I]B^{-1}F_1 \\ Y_3/S_3 &= e^{B\Delta}[Y_2/S_2]C_2 + [e^{B\Delta} - I]B^{-1}F_2 \\ &\dots \\ Y_{m+1}/S_{m+1} &= e^{B\Delta}[Y_m/S_m]C_m + [e^{B\Delta} - I]B^{-1}F_m \end{aligned} \quad (8)$$

Algebraic manipulation of eq 8 leads to the recursive formulas for  $Y_1, Y_2, \dots, Y_M$  representing the NMR signals produced by the model, which can be directly compared to the recorded data (where available; only a subset of simulated data points have corresponding experimental data as detailed above) and used for parameter estimation procedures:

$$\begin{aligned} Y_1 &= e^{B\Delta}[Y_0/S_0]C_0S_1 + [e^{B\Delta} - I]B^{-1}F_0S_1 \\ Y_2 &= e^{B\Delta}[Y_1/S_1]C_1S_2 + [e^{B\Delta} - I]B^{-1}F_1S_2 \\ Y_3 &= e^{B\Delta}[Y_2/S_2]C_2S_3 + [e^{B\Delta} - I]B^{-1}F_2S_3 \\ &\dots \\ Y_{m+1} &= e^{B\Delta}[Y_m/S_m]C_mS_{m+1} + [e^{B\Delta} - I]B^{-1}F_mS_{m+1} \end{aligned} \quad (9)$$

Some of the  $K$  elements of the vector  $Y$  (and therefore  $X$ ) may not be observed in the experiment and measured directly (for example, DHAP; described in subsequent sections), but they

can and should be included in the system as intermediate processes exert complete control over the observed metabolites.

**Model Matrix B.** The system of equations is defined by the rate matrix  $B$ . This matrix consists of the difference between the first order reaction rate constant matrix  $A_1$  and the spin-lattice relaxation rate matrix  $A_2$ . The relationship has the form:  $B = A_1 - A_2$ .

The rate constant matrix  $A_1$  describes the conversion between different metabolites involved in glucose metabolism as probed using  $[2-^{13}\text{C}]$  DHA. The relaxation matrix  $A_2$  models the signal decay due to spin-lattice relaxation. The metabolites observed in the NMR spectra are in the following order in equations:

$$\begin{pmatrix} \text{DHA} \\ \text{DHAP} \\ \text{GA3P} \\ \text{2GluP} \\ \text{2Glu} \\ \text{5GluP} \\ \text{5Glu} \\ \text{3PG} \\ \text{PEP} \\ \text{Pyr} \\ \text{Lac} \\ \text{Ala} \\ \text{G3P} \\ \text{Gly} \end{pmatrix} \quad (10)$$

In the  $^{13}\text{C}$  spectra, all the species defined in 10 were observed except DHAP. The reaction rate matrix is built based on the metabolic fate of each species in liver. This matrix,  $A_1$ , has the form:

$$A_1 = \begin{pmatrix} -k_1 & 0 & 0 & 0 & 0 & 0 & 0 & 0 & 0 & 0 & 0 & 0 & 0 & 0 \\ k_1 & -k_4 - k_2 - k_{10} & 0 & 0 & 0 & 0 & 0 & 0 & 0 & 0 & 0 & 0 & 0 & 0 \\ 0 & k_4 & -k_5 - k_2 & 0 & 0 & 0 & 0 & 0 & 0 & 0 & 0 & 0 & 0 & 0 \\ 0 & k_2 & 0 & -k_3 & 0 & 0 & 0 & 0 & 0 & 0 & 0 & 0 & 0 & 0 \\ 0 & 0 & 0 & k_3 & 0 & 0 & 0 & 0 & 0 & 0 & 0 & 0 & 0 & 0 \\ 0 & 0 & k_2 & 0 & 0 & -k_3 & 0 & 0 & 0 & 0 & 0 & 0 & 0 & 0 \\ 0 & 0 & 0 & 0 & 0 & k_3 & 0 & 0 & 0 & 0 & 0 & 0 & 0 & 0 \\ 0 & 0 & k_5 & 0 & 0 & 0 & 0 & -k_6 & 0 & 0 & 0 & 0 & 0 & 0 \\ 0 & 0 & 0 & 0 & 0 & 0 & 0 & k_6 & -k_7 & 0 & 0 & 0 & 0 & 0 \\ 0 & 0 & 0 & 0 & 0 & 0 & 0 & 0 & k_7 & -k_8 - k_9 & 0 & 0 & 0 & 0 \\ 0 & 0 & 0 & 0 & 0 & 0 & 0 & 0 & 0 & k_8 & 0 & 0 & 0 & 0 \\ 0 & 0 & 0 & 0 & 0 & 0 & 0 & 0 & 0 & k_9 & 0 & 0 & 0 & 0 \\ 0 & k_{10} & 0 & 0 & 0 & 0 & 0 & 0 & 0 & 0 & 0 & 0 & -k_{11} & 0 \\ 0 & 0 & 0 & 0 & 0 & 0 & 0 & 0 & 0 & 0 & 0 & 0 & k_{11} & 0 \end{pmatrix}$$

To account for signal decay due to spin–lattice relaxation, diagonal matrix  $A_2$  is defined for each signal that is included in the model.  $A_2$  takes the form shown below. The exact values for relaxation rates can either be experimentally determined or inferred by fitting the recorded HP data.

$$A_2 = \begin{pmatrix} \frac{1}{32} & 0 & 0 & 0 & 0 & 0 & 0 & 0 & 0 & 0 & 0 & 0 & 0 & 0 & 0 \\ 0 & \frac{1}{32} & 0 & 0 & 0 & 0 & 0 & 0 & 0 & 0 & 0 & 0 & 0 & 0 & 0 \\ 0 & 0 & \frac{1}{5} & 0 & 0 & 0 & 0 & 0 & 0 & 0 & 0 & 0 & 0 & 0 & 0 \\ 0 & 0 & 0 & \frac{1}{3} & 0 & 0 & 0 & 0 & 0 & 0 & 0 & 0 & 0 & 0 & 0 \\ 0 & 0 & 0 & 0 & \frac{1}{3} & 0 & 0 & 0 & 0 & 0 & 0 & 0 & 0 & 0 & 0 \\ 0 & 0 & 0 & 0 & 0 & \frac{1}{3} & 0 & 0 & 0 & 0 & 0 & 0 & 0 & 0 & 0 \\ 0 & 0 & 0 & 0 & 0 & 0 & \frac{1}{3} & 0 & 0 & 0 & 0 & 0 & 0 & 0 & 0 \\ 0 & 0 & 0 & 0 & 0 & 0 & 0 & \frac{1}{30} & 0 & 0 & 0 & 0 & 0 & 0 & 0 \\ 0 & 0 & 0 & 0 & 0 & 0 & 0 & 0 & \frac{1}{30} & 0 & 0 & 0 & 0 & 0 & 0 \\ 0 & 0 & 0 & 0 & 0 & 0 & 0 & 0 & 0 & \frac{1}{5.5} & 0 & 0 & 0 & 0 & 0 \\ 0 & 0 & 0 & 0 & 0 & 0 & 0 & 0 & 0 & 0 & \frac{1}{5} & 0 & 0 & 0 & 0 \\ 0 & 0 & 0 & 0 & 0 & 0 & 0 & 0 & 0 & 0 & 0 & \frac{1}{3} & 0 & 0 & 0 \\ 0 & 0 & 0 & 0 & 0 & 0 & 0 & 0 & 0 & 0 & 0 & 0 & \frac{1}{3} & 0 & 0 \end{pmatrix}$$

**Substrate Delivery and Utilization.** Introduction of hyperpolarized dihydroxyacetone to the livers can be modeled using the rescaled gamma distribution density.<sup>18</sup> The delivery of DHA has the parametric form

$$\text{DHA}(t) = Ct^{\alpha-1}e^{-\beta t} \quad (11)$$

The parameters  $C$ ,  $\alpha$ , and  $\beta$  are estimated from fitting gamma curve  $\text{DHA}(t)$  to observed DHA signal intensities at time points  $t_0, t_1, t_2, \dots, t_N$ .

The delivery function models the total DHA in the system and does not account for the fraction of DHA that is actively metabolized by the liver. The fraction utilized by the liver acts as the driving force for the metabolic activity involving DHA. This driving force ( $F(t)$ ), which has a single nonzero vector component representing the DHA influx into the liver, is defined as

$$F(t) = \begin{pmatrix} F_1(t) \\ 0 \\ 0 \\ 0 \\ 0 \\ 0 \\ 0 \\ 0 \\ 0 \\ 0 \\ 0 \\ 0 \\ 0 \\ 0 \\ 0 \end{pmatrix}$$

where  $F_1(t)$  represents the uptake of HP DHA by the liver.

To model values for each time point in the HP experiment, parametric modeling of  $F_1(t)$  can be utilized. With total DHA concentration as a baseline, the driving force of DHA metabolism for  $F(t)$  can be inferred.

Fractional utilization of DHA ( $F_1(t)$ ) can be estimated by using the values of parameters  $C$ ,  $\alpha$ , and  $\beta$  from fitting eq 11 along with three additional parameters  $a_1, a_2, a_3$  in the form given in equation below:

$$F_1(t) = a_1 \text{DHA}(a_2 t + a_3) = a_1 C (a_2 t + a_3)^{\alpha-1} e^{-\beta(a_2 t + a_3)} \quad (12)$$

**Summary of Parameters.** The parameters describing the fractional utilization ( $a_1, a_2, a_3$ ) are estimated in the minimization algorithm together with the reaction rate constants ( $k_i$ 's) making the total number of parameters equal to 14. Those parameters used to describe the temporal evolution of HP DHA signals ( $C, \alpha$ , and  $\beta$ ; see eq 11) are estimated prior to the model fitting and are not included in the count of 14 parameters.

## RESULTS AND DISCUSSION

Dihydroxyacetone is avidly consumed by the liver and has several different metabolic fates as shown in Figure 1. The metabolites generated by the tissue from DHA have different spin relaxation properties, and hence, a multistep modeling approach is needed. Steps involved in modeling DHA kinetics and relaxation data from each mouse is shown in Figure 2. Rescaled peak areas (estimation detailed in Methods) were used without further modification for comparison with model output. As the first step, it is necessary to estimate spin–lattice relaxation rates of different metabolites involved in the reaction. Although spin–lattice relaxation rates can be experimentally determined *in vitro*, these values are often different from those of metabolites in tissue. In this analysis, we estimate the relaxation parameters from the NMR spectra (Figure 2).

Values for spin–lattice relaxation times used in the model (Matrix  $A_2$ ) and those obtained from the data using the model are shown in Table 1. As shown in Figure 2a, spin–lattice relaxation rates are initial assumed for estimating the kinetic rate constants ( $k_i$ 's) and other model parameters. Using the model estimated parameters, values for spin–lattice relaxation times are re-estimated by comparing the model output to peak areas from HP spectra. A comparison between initial and

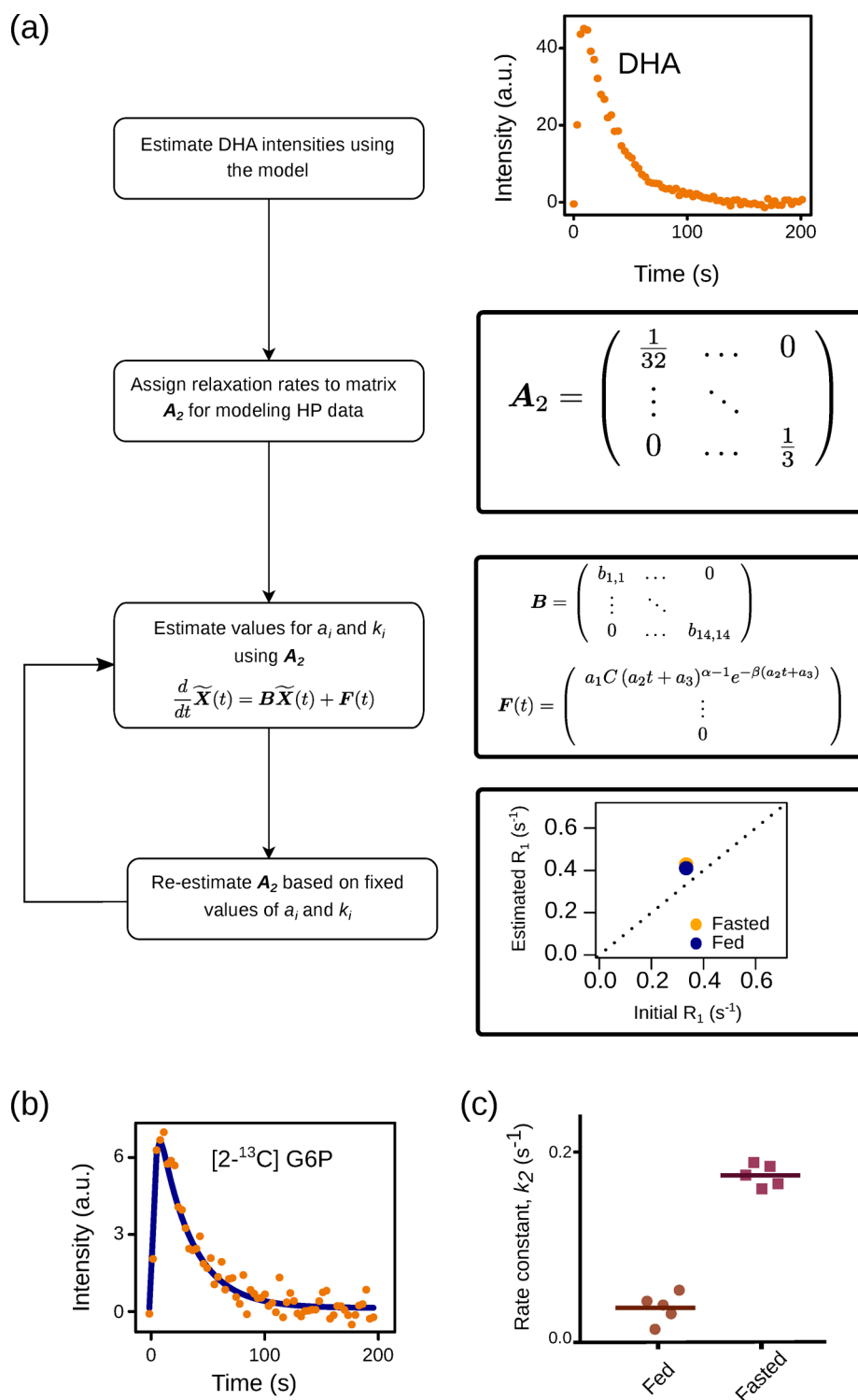


**Figure 2.** (a) Flowchart describing the modeling approach. Complete forms of the matrices are detailed in the [Methods](#) section. (b) Comparison of HP data (orange dots) and model output (blue line). (c) Kinetic rate constant,  $k_2$ , estimated using model. Filled dots and squares indicate values from individual experiments. Horizontal line indicates mean.  $n = 5$  each for fed and fasted.

estimated spin relaxation rates for three metabolites (positioned at different branches of DHA in metabolism) is shown in [Figure 3](#). It is interesting that relaxation times for DHA are very different between the initial and estimated values. This is likely due to DHA being present both inside the liver and in the solution surrounding it. This presents DHA from multiple different environments during analysis. Since a large excess is

injected and only a fraction is taken up by the liver, it is likely that the estimated values are dominated by the population of DHA in solution and not inside the tissue. This argument is strengthened when the relaxation rates of LAC are compared. Since, all LAC is likely to be present inside the tissue and not elsewhere, the relaxation values represent LAC in a single environment. This can also be seen for most of the other metabolites.

**Table 1.** Initial Spin–Lattice Relaxation Times of Metabolites in the EMP Pathway Used in the Model

metabolites	spin–lattice relaxation time (s)	
	initial	estimated
DHA	32 <sup>17</sup>	65
DHAP	32	36
GA3P	5.0	3.1
2-GluP	3.0	1.9
2-Glu	3.0	2.8
5-GluP	3.0	2.6
5-Glu	3.0	3.1
3PG	3.0	3.9
PEP	30	15
Pyr	30	16
Lac	5.5	6.8
Ala	5.0	5.5
G3P	3.0	2.4
Gly	3.0	3.1

Incorporating the estimated relaxation rates in the model (yielding an updated matrix  $A_2$ ; indicated as “Estimated” in Table 1), peak areas from NMR spectra are fit again. Model output and fit residuals are shown in Figure 4 for lactate (LAC), glycerol-3-phosphate (G3P), and [2-<sup>13</sup>C]glucose-6-phosphate (G6P). It is evident from the fits that even the lower intensity peaks such as lactate are described by the model faithfully. Fits and residuals for all the metabolites (from a single HP experiment) included in the model are shown in Figures S2 and S3.

NMR measurements of dynamic processes yield signals that are a function of chemical kinetics, RF excitation, and spin–lattice relaxation. In the case of HP experiments, another factor, substrate delivery, needs to be considered as well. The delivery of hyperpolarized substrates introduces additional modeling considerations. The delivery function can be described using two major components—(1) macroscopic injection of the HP substrates and (2) the uptake of the substrates by the tissue under consideration. Since the time taken for the macroscopic injection is typically orders of magnitude longer than the cellular uptake, the latter can be assumed to be instantaneous. However, the amount of hyperpolarized substrate that is injected is in large excess of what is utilized by the tissues. Therefore, fractional utilization of the substrate has to be accounted for during modeling the signal intensities. In these experiments, a large excess of HP [2-<sup>13</sup>C] DHA is injected into the liver. It is

inconceivable that all the DHA is consumed by the liver owing to the short duration of the experiment and hence the incongruity between the observed DHA signal intensities and the model output (Figure S1).

<sup>13</sup>C signals from the metabolites generated from HP [2-<sup>13</sup>C] DHA can, however, be modeled accurately since the contribution of hyperpolarized <sup>13</sup>C signal far outweighs natural abundance <sup>13</sup>C signal (natural abundance of <sup>13</sup>C is 1.1%). This can be seen from Figure 4 (top panels) and Figure S2. Residuals (Figure 4 (bottom panels) and Figure S3), computed as the ratio of difference between model output and experimental values to its standard deviation, show good agreement between the model and peak areas. Since the residuals are not bound, the magnitude indicates variability in the fit quality between different chemical species. It can be seen that signal intensities of most species can be accurately described in the model.

In addition to the spin relaxation values, reaction rate constants of several individual reactions were also obtained from the model. Since not all metabolic intermediates were observed (e.g., 2-phosphoglycerate and fructose-1,6-bisphosphate), some of the rate constants estimated are composite rate constants describing more than one enzymatic step, except in the special case of DHAP. Although DHAP is not observed in the experiment, it has multiple fates (Figure 1) and hence the need for explicit inclusion in the model. This is done to avoid spurious fitting of the branches in DHAP consumption (glycerol-3-phosphate and glyceraldehyde-3-phosphate). Kinetic rate constants obtained from the data are shown in Figure 5. It is possible to estimate rate constants over a wide range ( $2 \times 10^{-3} \text{ s}^{-1}$  for  $k_9$  (fasted) to  $2.4 \text{ s}^{-1}$  for  $k_6$  (fed)) using this approach.

Estimated kinetic rate constants show some interesting differences between the two physiological states under comparison. In the gluconeogenic (fasted) state, it would be expected that the gluconeogenic segment of DHA metabolism have higher reaction rates. Indeed, values of the composite rate constant describing the synthesis of glucose-6-phosphate from DHAP and glyceraldehyde-3-phosphate ( $k_2$ ) is significantly higher ( $p \ll 0.05$ ) in fasted than fed state. In contrast, the rate constants associated with precursors for fatty acid synthesis (glycerol and G3P) have higher reaction rates in the fed state ( $k_{10}$  and  $k_{11}$ ). These results are in agreement with other studies that have reported fatty acid synthesis in perfused fed livers.<sup>25,26</sup> Interestingly, the exchange rates between pyruvate–lactate and

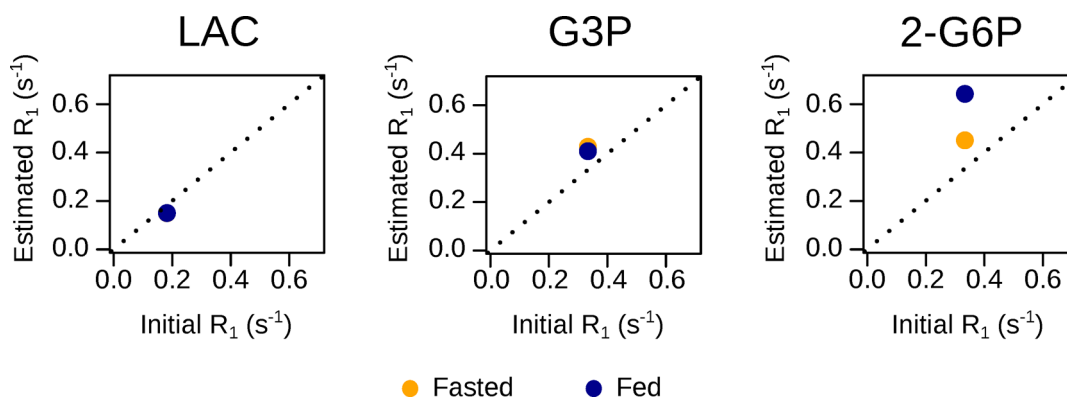


**Figure 3.** Comparison of initial and estimated spin–lattice relaxation rates.  $R_1$  values of lactate (LAC), glycerol-3-phosphate (G3P) and [2-<sup>13</sup>C]glucose-6-phosphate (2-G6P) are shown in the plots. These three metabolites represent three different segments of DHA metabolism—glycolysis (LAC), gluconeogenesis ([2-<sup>13</sup>C] G6P), and fatty acid synthesis (G3P).

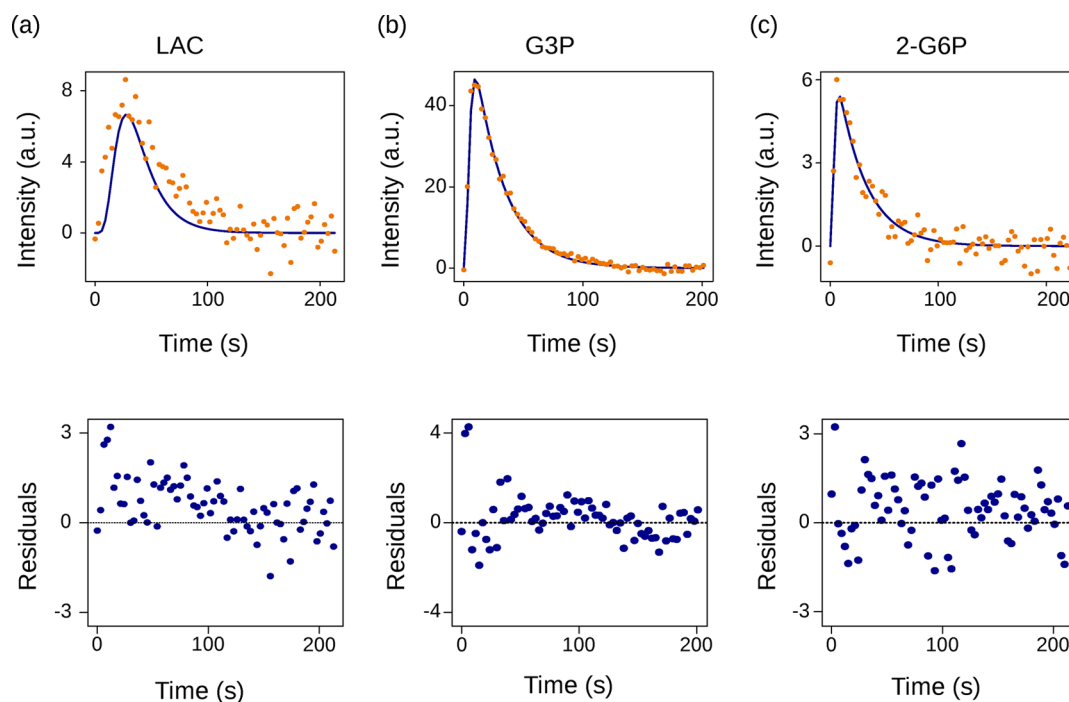


**Figure 4.** Model output (top) and residuals (bottom) for (a) lactate (LAC), (b) glycerol-3-phosphate (G3P) and (c) [2-<sup>13</sup>C] glucose-6-phosphate (2-G6P). In the model outputs, orange filled dots indicate experimental data (peak areas) and solid blue lines indicate model output. Residuals were calculated as a ratio of difference between model output and experimental values to its standard deviation.

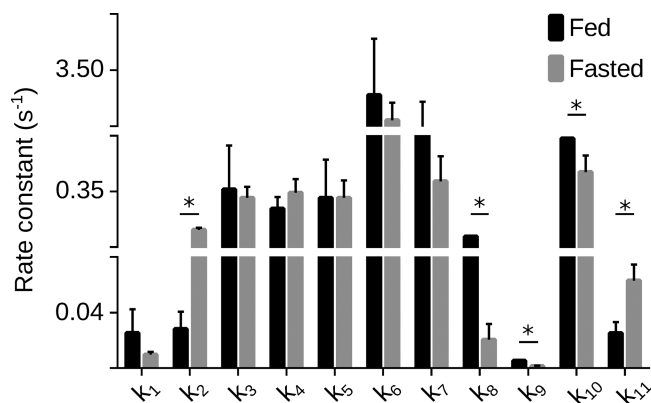


**Figure 5.** Comparison of reaction rate constants of various steps in DHA metabolism between and fed and fasted states. Error bars indicate standard deviation. Significant differences ( $p < 0.05$ ) are indicated with \*.  $n = 5$  for each group.

pyruvate–alanine pairs were lower ( $p < 0.05$ ) in fasted livers. Perfusions of fasted livers were carried out in the presence of 2 mM pyruvate. This results in competition between pyruvate from the perfusate and pyruvate generated from HP [2-<sup>13</sup>C] DHA. However, <sup>13</sup>C signals from unlabeled pyruvate are not observed thereby underestimating the rates of pyruvate–lactate and pyruvate–alanine exchange reactions.

Several approaches exist for modeling dynamic NMR data such as those obtained from HP experiments.<sup>18–21</sup> Two of these approaches do not involve directly fitting peak areas and are discussed here. A model-free formalism described by Hill et al.<sup>27</sup> describes the forward rate constant of a HP substrate to one or more products as ratio of area under the curves (AUC) of the substrate to the product. In this formalism, however, the products undergoing subsequent reactions are not defined. It is unclear how that affects the AUC of the products (substrates in

subsequent steps) and, hence, may not be directly applicable to modeling DHA kinetics. In our model, we were able to include almost all the metabolites in the pathway explicitly for kinetic estimation. Further, we were able to model even those resonances that are missing in a subset of experiments (see [Methods](#)).

Another approach to estimation of kinetic parameters involves utilizing line width of the product resonances.<sup>28</sup> However, an important assumption in this model is that the reactant and product apparent spin–lattice relaxation values are roughly equal. In the case of DHA metabolism, spin relaxation times range from ~36 to ~2s. Another complication arises from signal-to-noise (S/N) consideration of the product resonances. Since some metabolites from hepatic metabolism of DHA have low S/N ratios, accurate estimation of peak widths is problematic and a likely source of error. Although S/N considerations are practically universal in any modeling approach, our results suggest that the model we have presented performs well even for the low intensity peaks with minimal manual intervention.

Although the model formulation presented here is applicable for a wide range of experimental designs and metabolic probes, *in vivo* measurements will necessitate inclusion of additional parameters for accurate estimation of model parameters. For example, in a model describing hyperpolarized pyruvate kinetics, Zierhut et al., explicitly accounted for the rate and time of appearance of HP pyruvate signal since these parameters are confounded by both the injection rate and circulation.<sup>29</sup> For *in vivo* experiments, transit of the vascular bed might also be an essential part of the model.<sup>18</sup> Further, if spatiotemporal resolution is available (e.g., HP MR imaging), extensive modeling approaches available in the PET imaging literature<sup>30–33</sup> can be utilized to extend the model presented in this work to *in vivo* studies.

Diseases such as diabetes have altered kinetics of various metabolic pathways including gluconeogenesis. Suggested

treatment methods have included approaches which alter the kinetics of specific pathways (e.g., PDH).<sup>34,35</sup> HP [ $2-^{13}\text{C}$ ] DHA provides the means to probe several pathways involved in carbohydrate metabolism. Using the model presented here, we can extract useful kinetic information thereby informing on disease progression and efficacy of treatment.

## CONCLUSION

In summary, we have presented a model to describe both the relaxation and kinetic components of a metabolic reaction of a hyperpolarized substrate that has multiple metabolic fates. We can extract reaction rate constants corresponding to almost all observable products. Further, we are able to differentiate the rates between different physiological states based on the model output. This has wide applicability in monitoring metabolic disease progression and potentially, treatment of those disorders.

## ASSOCIATED CONTENT

### Supporting Information

The Supporting Information is available free of charge on the ACS Publications website at DOI: 10.1021/acs.jcim.8b00745.

Additional figures (PDF)

## AUTHOR INFORMATION

### Corresponding Author

\*E-mail: matthewmerritt@ufl.edu.

### ORCID

Mukundan Ragavan: 0000-0001-8678-4229

Matthew E. Merritt: 0000-0003-4617-9651

### Author Contributions

<sup>○</sup>These authors contributed equally.

### Notes

The authors declare no competing financial interest.

## ACKNOWLEDGMENTS

This work was funded by National Institutes of Health (NIH) grants R01-DK-105346, R01-HD-087306, R01-DK-112865, P41-122698, and U24-DK-097209. A.K. was supported by University of Florida Informatics Institute Fellowship. A portion of this work was performed at the National High Magnetic Field Laboratory, which is supported by National Science Foundation Cooperative Agreement No. DMR-1644779 and the State of Florida. J.A.B. was supported by funds from NIH grant R01-CA-211150.

## REFERENCES

- (1) Beckonert, O.; Keun, H. C.; Ebbels, T. M. D.; Bundy, J.; Holmes, E.; Lindon, J. C.; Nicholson, J. K. Metabolic profiling, metabolomic and metabonomic procedures for NMR spectroscopy of urine, plasma, serum and tissue extracts. *Nat. Protoc.* **2007**, *2*, 2692.
- (2) Bertram, H. C.; Knudsen, K. E. B.; Serena, A.; Malmendal, A.; Nielsen, N. C.; Fretté, X. C.; Andersen, H. J. NMR-based metabonomic studies reveal changes in the biochemical profile of plasma and urine from pigs fed high-fibre rye bread. *Br. J. Nutr.* **2006**, *95*, 955–962.
- (3) Chance, E. M.; Seeholzer, S. H.; Kobayashi, K.; Williamson, J. R. Mathematical analysis of isotope labeling in the citric acid cycle with applications to  $^{13}\text{C}$  NMR studies in perfused rat hearts. *J. Biol. Chem.* **1983**, *258*, 13785–13794.
- (4) Ardenkjær-Larsen, J. H.; Fridlund, B.; Gram, A.; Hansson, G.; Hansson, L.; Lerche, M. H.; Servin, R.; Thaning, M.; Golman, K.

Increase in signal-to-noise ratio of > 10,000 times in liquid-state NMR. *Proc. Natl. Acad. Sci. U. S. A.* **2003**, *100*, 10158–10163.

- (5) Schroeder, M. A.; Lau, A. Z.; Chen, A. P.; Gu, Y.; Nagendran, J.; Barry, J.; Hu, X.; Dyck, J. R.; Tyler, D. J.; Clarke, K.; Connelly, K. A.; Wright, G. A.; Cunningham, C. H. Hyperpolarized  $^{13}\text{C}$  magnetic resonance reveals early- and late-onset changes to *in vivo* pyruvate metabolism in the failing heart. *Eur. J. Heart Failure* **2013**, *15*, 130–140.

- (6) Nelson, S. J.; Kurhanewicz, J.; Vigneron, D. B.; Larson, P. E. Z.; Harzstark, A. L.; Ferrone, M.; Criekinge, M. v.; Chang, J. W.; Bok, R.; Park, I.; Reed, G.; Carvajal, L.; Small, E. J.; Munster, P.; Weinberg, V. K.; Ardenkjær-Larsen, J. H.; Chen, A. P.; Hurd, R. E.; Odegardstuen, L.-I.; Robb, F. J.; Tropp, J.; Murray, J. A. Metabolic Imaging of Patients with Prostate Cancer Using Hyperpolarized [ $1-^{13}\text{C}$ ]Pyruvate. *Sci. Transl. Med.* **2013**, *5*, 198ra108.

- (7) Keshari, K. R.; Sriram, R.; Koelsch, B. L.; Crieckinge, M. V.; Wilson, D. M.; Kurhanewicz, J.; Wang, Z. J. Hyperpolarized  $^{13}\text{C}$ -pyruvate magnetic resonance reveals rapid lactate export in metastatic renal cell carcinomas. *Cancer Res.* **2013**, *73*, 529–538.

- (8) Lau, A. Z.; Chen, A. P.; Ghugre, N. R.; Ramanan, V.; Lam, W. W.; Connelly, K. A.; Wright, G. A.; Cunningham, C. H. Rapid multislice imaging of hyperpolarized  $^{13}\text{C}$  pyruvate and bicarbonate in the heart. *Magn. Reson. Med.* **2010**, *64*, 1323–1331.

- (9) Schroeder, M. A.; Atherton, H. J.; Ball, D. R.; Cole, M. A.; Heather, L. C.; Griffin, J. L.; Clarke, K.; Radda, G. K.; Tyler, D. J. Real-time assessment of Krebs cycle metabolism using hyperpolarized  $^{13}\text{C}$  magnetic resonance spectroscopy. *FASEB J.* **2009**, *23*, 2529–2538.

- (10) Golman, K.; Zandt, R. i.; Lerche, M.; Pehrson, R.; Ardenkjær-Larsen, J. H. Metabolic Imaging by Hyperpolarized  $^{13}\text{C}$  Magnetic Resonance Imaging for In vivo Tumor Diagnosis. *Cancer Res.* **2006**, *66*, 10855–10860.

- (11) Bastiaansen, J. A. M.; Yoshihara, H. A. I.; Takado, Y.; Gruetter, R.; Comment, A. Hyperpolarized  $^{13}\text{C}$  lactate as a substrate for *in vivo* metabolic studies in skeletal muscle. *Metabolomics* **2014**, *10*, 986–994.

- (12) Ball, D. R.; Rowlands, B.; Dodd, M. S.; Le Page, L.; Ball, V.; Carr, C. A.; Clarke, K.; Tyler, D. J. Hyperpolarized butyrate: A metabolic probe of short chain fatty acid metabolism in the heart: Hyperpolarized Butyrate, A Probe of Short Chain Fatty Acid Metabolism. *Magn. Reson. Med.* **2014**, *71*, 1663–1669.

- (13) Bastiaansen, J. A. M.; Merritt, M. E.; Comment, A. Measuring changes in substrate utilization in the myocardium in response to fasting using hyperpolarized [ $1-^{13}\text{C}$ ]butyrate and [ $1-^{13}\text{C}$ ]pyruvate. *Sci. Rep.* **2016**, *6*, 25573.

- (14) von Morze, C. v.; Ohliger, M. A.; Marco-Rius, I.; Wilson, D. M.; Flavell, R. R.; Pearce, D.; Vigneron, D. B.; Kurhanewicz, J.; Wang, Z. J. Direct assessment of renal mitochondrial redox state using hyperpolarized  $^{13}\text{C}$ -acetoacetate. *Magn. Reson. Med.* **2018**, *79*, 1862–1869.

- (15) Cabella, C.; Karlsson, M.; Canapè, C.; Catanzaro, G.; Colombo Serra, S.; Miragoli, L.; Poggi, L.; Uggeri, F.; Venturi, L.; Jensen, P. R.; Lerche, M. H.; Tedoldi, F. In vivo and in vitro liver cancer metabolism observed with hyperpolarized [ $5-^{13}\text{C}$ ]glutamine. *J. Magn. Reson.* **2013**, *232*, 45–52.

- (16) Comment, A.; Merritt, M. E. Hyperpolarized Magnetic Resonance as a Sensitive Detector of Metabolic Function. *Biochemistry* **2014**, *53*, 7333–7357.

- (17) Moreno, K. X.; Satapati, S.; DeBerardinis, R. J.; Burgess, S. C.; Malloy, C. R.; Merritt, M. E. Real-time Detection of Hepatic Gluconeogenic and Glycogenolytic States Using Hyperpolarized [ $2-^{13}\text{C}$ ] Dihydroxyacetone. *J. Biol. Chem.* **2014**, *289*, 35859–35867.

- (18) Bankson, J. A.; Walker, C. M.; Ramirez, M. S.; Stefan, W.; Fuentes, D.; Merritt, M. E.; Lee, J.; Sandulache, V. C.; Chen, Y.; Phan, L.; Chou, P.-C.; Rao, A.; Yeung, S.-C. J.; Lee, M.-H.; Schellingerhout, D.; Conrad, C. A.; Malloy, C.; Sherry, A. D.; Lai, S. Y.; Hazle, J. D. Kinetic Modeling and Constrained Reconstruction of Hyperpolarized [ $1-^{13}\text{C}$ ]Pyruvate Offers Improved Metabolic Imaging of Tumors. *Cancer Res.* **2015**, *75*, 4708–4717.

- (19) Bahrami, N.; Swisher, C. L.; Von Morze, C.; Vigneron, D. B.; Larson, P. E. Z. Kinetic and perfusion modeling of hyperpolarized  $^{13}\text{C}$  pyruvate and urea in cancer with arbitrary RF flip angles. *Quant Imaging Med. Surg* **2014**, *4*, 24–32.
- (20) Kazan, S. M.; Reynolds, S.; Kennerley, A.; Wholey, E.; Bluff, J. E.; Berwick, J.; Cunningham, V. J.; Paley, M. N.; Tozer, G. M. Kinetic modeling of hyperpolarized  $^{13}\text{C}$  pyruvate metabolism in tumors using a measured arterial input function. *Magn. Reson. Med.* **2013**, *70*, 943–953.
- (21) Witney, T. H.; Kettunen, M. I.; Brindle, K. M. Kinetic modeling of hyperpolarized  $^{13}\text{C}$  label exchange between pyruvate and lactate in tumor cells. *J. Biol. Chem.* **2011**, *286*, 24572.
- (22) Albers, M. J.; Bok, R.; Chen, A. P.; Cunningham, C. H.; Zierhut, M. L.; Zhang, V. Y.; Kohler, S. J.; Tropp, J.; Hurd, R. E.; Yen, Y.-F.; Nelson, S. J.; Vigneron, D. B.; Kurhanewicz, J. Hyperpolarized  $^{13}\text{C}$  Lactate, Pyruvate, and Alanine: Noninvasive Biomarkers for Prostate Cancer Detection and Grading. *Cancer Res.* **2008**, *68*, 8607–8615.
- (23) Dessau, R.; Pipper, C. B. “R”-project for statistical computing. *Ugeskrift for læger* **2008**, *170*, 328–330.
- (24) Harrison, C.; Yang, C.; Jindal, A.; DeBerardinis, R. J.; Hooshyar, M.; Merritt, M.; Dean Sherry, A.; Malloy, C. R. Comparison of kinetic models for analysis of pyruvate-to-lactate exchange by hyperpolarized  $^{13}\text{C}$  NMR. *NMR Biomed.* **2012**, *25*, 1286–1294.
- (25) Salmon, D. M. W.; Bowen, N. L.; Hems, D. A. Synthesis of fatty acids in the perfused mouse liver. *Biochem. J.* **1974**, *142*, 611–618.
- (26) Wadke, M.; Brunengraber, H.; Lowenstein, J. M.; Dolhun, J. J.; Arsenault, G. P. Fatty acid synthesis by the liver perfused with deuterated and tritiated water. *Biochemistry* **1973**, *12*, 2619–2624.
- (27) Hill, D. K.; Orton, M. R.; Mariotti, E.; Boulton, J. K. R.; Panek, R.; Jafar, M.; Parkes, H. G.; Jamin, Y.; Miniotis, M. F.; Al-Saffar, N. M. S.; Belouche-Babari, M.; Robinson, S. P.; Leach, M. O.; Chung, Y.-L.; Eykyn, T. R. Model Free Approach to Kinetic Analysis of Real-Time Hyperpolarized  $^{13}\text{C}$  Magnetic Resonance Spectroscopy Data. *PLoS One* **2013**, *8*, No. e71996.
- (28) Pagés, G.; Kuchel, P. W. FmRα analysis: Rapid and direct estimation of relaxation and kinetic parameters from dynamic nuclear polarization time courses. *Magn. Reson. Med.* **2015**, *73*, 2075–2080.
- (29) Zierhut, M. L.; Yen, Y.-F.; Chen, A. P.; Bok, R.; Albers, M. J.; Zhang, V.; Tropp, J.; Park, I.; Vigneron, D. B.; Kurhanewicz, J.; Hurd, R. E.; Nelson, S. J. Kinetic modeling of hyperpolarized  $^{13}\text{C}_1$ -pyruvate metabolism in normal rats and TRAMP mice. *J. Magn. Reson.* **2010**, *202*, 85–92.
- (30) Garbarino, S.; Vivaldi, V.; Delbary, F.; Caviglia, G.; Piana, M.; Marini, C.; Capitanio, S.; Calamia, I.; Buschiazzo, A.; Sambucetti, G. A new compartmental method for the analysis of liver FDG kinetics in small animal models. *EJNMMI Res.* **2015**, *5*, 35.
- (31) Keiding, S. Bringing Physiology into PET of the Liver. *J. Nucl. Med.* **2012**, *53*, 425–433.
- (32) Munk, O. L.; Bass, L.; Roelsgaard, K.; Bender, D.; Hansen, S. B.; Keiding, S. Liver Kinetics of Glucose Analogs Measured in Pigs by PET: Importance of Dual-Input Blood Sampling. *J. Nucl. Med.* **2001**, *42*, 795–801.
- (33) Gunn, R. N.; Gunn, S. R.; Turkheimer, F. E.; Aston, J. A. D.; Cunningham, V. J. Positron Emission Tomography Compartmental Models: A Basis Pursuit Strategy for Kinetic Modeling. *J. Cereb. Blood Flow Metab.* **2002**, *22*, 1425–1439.
- (34) Madiraju, A. K.; Erion, D. M.; Rahimi, Y.; Zhang, X.-M.; Braddock, D. T.; Albright, R. A.; Prigaro, B. J.; Wood, J. L.; Bhanot, S.; MacDonald, M. J.; Jurczak, M. J.; Camporez, J.-P.; Lee, H.-Y.; Cline, G. W.; Samuel, V. T.; Kibbey, R. G.; Shulman, G. I. Metformin suppresses gluconeogenesis by inhibiting mitochondrial glycerophosphate dehydrogenase. *Nature* **2014**, *510*, 542–546.
- (35) Le Page, L. M. L.; Rider, O. J.; Lewis, A. J.; Ball, V.; Clarke, K.; Johansson, E.; Carr, C. A.; Heather, L. C.; Tyler, D. J. Increasing Pyruvate Dehydrogenase Flux as a Treatment for Diabetic Cardiomyopathy: A Combined  $^{13}\text{C}$  Hyperpolarized Magnetic Resonance and Echocardiography Study. *Diabetes* **2015**, *64*, 2735–2743.